

Collective Oscillations of Bose-Einstein Condensates in a Synthetic Magnetic Field

Huaxin He,^{1,*} Fengtao Pang,^{1,*} Yongping Zhang,^{1,†} and Chunlei Qu^{2,3,‡}

¹*Institute for Quantum Science and Technology, Department of Physics, Shanghai University, Shanghai 200444, China*

²*Department of Physics, Stevens Institute of Technology, Hoboken, NJ 07030, USA*

³*Center for Quantum Science and Engineering, Stevens Institute of Technology, Hoboken, NJ 07030, USA*

We study the collective oscillations of spin-orbit-coupled Bose-Einstein condensates in the presence of position-dependent detuning. Specifically, we explore the quadrupole modes of the system using both numerical and analytical approaches based on the Gross-Pitaevskii equation and hydrodynamic theory. Due to spin-orbit coupling and the synthetic magnetic field, the xy scissors mode couples with a superposition of the three diagonal quadrupole modes (x^2 , y^2 , and z^2), resulting in the characteristic beating effect. The remaining two scissors modes, xz and yz , are coupled, giving rise to a Lissajous-like pattern that is highly sensitive to the excitation method and orientation of the synthetic magnetic field. Furthermore, we find that anisotropic interactions as well as the direction of the synthetic magnetic field, can significantly influence the oscillation amplitude and frequency of the quadrupole modes. These findings highlight the potential of Bose-Einstein condensates under synthetic magnetic fields for quantum sensing applications, such as magnetic field gradient measurements, and provide a promising foundation for future experimental research and technological development.

I. INTRODUCTION

Ultracold atomic gases offer unparalleled controllability and flexibility, making them an ideal platform for quantum simulations to explore exotic states of matter [1–4]. Artificial gauge fields enable neutral atoms to mimic electrons in sensing electromagnetic fields, facilitating the investigation of synthetic magnetism and synthetic spin-orbit coupling (SOC) using ultracold atoms [5–11]. It is well known that magnetic fields and SOC are key origins of topological physics in solid-state electronic systems [12]. Ultracold atoms, when coupled with artificial gauge fields, offer a novel means to explore and substantiate various topological phenomena [13]. Notably, topological insulator models such as the Haldane model and SSH model have been successfully implemented in recent ultracold atom experiments, enabling the study of their topological properties with neutral atoms [14–19].

The rapid progress in SOC Bose-Einstein condensates (BEC) has stimulated extensive research into their exotic superfluid properties [20–43]. Compared to traditional BEC, SOC introduces a spin-dependent modification in the momentum operator, which fundamentally modifies the current-phase relationship [25, 26]. This modification leads to the violation of the rotational constraint of the velocity field [38], which arises due to the breaking of Galilean invariance induced by SOC [41, 42]. A direct consequence of this symmetry breaking is that the definition of the superfluid critical velocity depends on the observer’s reference frame [20], while the velocity field associated with the fluid rotation exhibits diffusive vorticity [38]. Beyond these fundamental changes in super-

fluidity, SOC BEC also exhibit novel quantum phases and dynamics. For instance, when the Raman coupling is weak, the atoms may occupy two momentum states, leading to the emergence of a stripe phase—a novel state that exhibits both crystalline-like order and superfluid behavior [33, 36, 43]. When Raman coupling is increased, the condensate may evolve from a plane-wave phase to a zero-momentum phase, where many interesting physical quantities diverge [21, 37]. Furthermore, introducing a position-dependent detuning into the SOC BEC system creates a synthetic magnetic field for neutral atoms [44], which imparts nonzero angular momentum and leads to a rigid-like rotational velocity field [39]. As the detuning gradient increases, vortices can be generated without the rotation of the confining trap [40], demonstrating a novel mechanism for vortex formation. These findings collectively highlight the rich interplay between SOC and superfluidity and open new avenues for exploring quantum many-body physics.

Collective modes play a crucial role in revealing fundamental properties of ultracold atomic gases, such as testing superfluidity, calibrating the frequency of trapping potentials, and detecting angular momentum [45–49]. The dynamics of SOC BEC in a synthetic magnetic field exhibit novel properties, including the precession of dipole oscillations, similar to a Foucault pendulum, and a Hall-like effect produced by quench dynamics [39, 50]. The synthetic magnetic field induces the coupling between the scissors and quadrupole modes leading to a notable beating effect and gyroscope-like dynamics [40]. Moreover, recent studies have uncovered an interesting spin-deflection effect by the rigid-like rotational velocity field during the expansion dynamics [51]. In exploring these collective dynamics, the recent work [40] has primarily focused on a specific parameter regime where the quadrupole modes in the plane perpendicular to the synthetic magnetic field are degenerate. Under the influence of synthetic magnetic fields, these degenerate modes ex-

* These authors contributed equally to this work.

† yongping11@t.shu.edu.cn

‡ cqu5@stevens.edu

hibit strong coupling, leading to pronounced collective dynamics.

In this paper, we systematically investigate collective oscillations of SOC BEC in a synthetic magnetic field by considering a broad parameter regime. Our results generalize the application of spinor hydrodynamic (HD) theory and are corroborated by the numerical simulation of the Gross-Pitaevskii equation (GPE). We find that various quadrupole modes are coupled with the scissors mode, resulting in a perfect beating effect in their collective oscillations. Additionally, the oscillation trajectories of the other two coupled scissors modes exhibit a feature similar to Lissajous patterns. Additionally, the oscillation trajectories of the other two coupled scissors modes resemble Lissajous patterns—trajectory curves generated by the combination of two harmonic vibrations that are perpendicular to each other [52, 53]. We have also extended our calculation to the system with anisotropic interactions between the two components, which are crucial for a general understanding of the real system. Additionally, we study the collective oscillation of the BEC in a synthetic magnetic field that points to an arbitrary direction. Our findings reveal that anisotropic interactions and the direction of synthetic magnetic fields significantly alter the oscillation amplitude, frequency, and coupling of these modes.

This paper is organized as follows. In Sec. II, we describe the basic model of the system and the derivation of the HD equations. In Sec. III, we study the coupling dynamics of quadrupole modes by comparing numerical simulations and analytical results from HD. In Sec. IV and V, the model is extended to more general cases, considering the effects of anisotropic interactions and different directions of synthetic magnetic fields on quadrupole mode coupling. Finally, Section VI provides a summary of the paper.

II. MODEL

We consider a spin-1/2 BEC of ^{87}Rb atoms at zero temperature, with an equal Rashba-Dresselhaus SOC induced along the x -direction by two-photon Raman coupling [8, 9, 54–56]. In the mean-field framework, the dynamics of the SOC BEC are governed by the (hereafter set $\hbar = 1$)

$$i\partial_t\psi = (H_0 + H_{\text{int}})\psi, \quad (1)$$

where $\psi = (\psi_1, \psi_2)^T$ represents the order parameter of the two components, satisfying the normalization condition $\int d\mathbf{r}|\psi|^2 = N$, with N denoting the total number of atoms. The two-body interactions between atoms are described by the nonlinear term $H_{\text{int}} = \text{diag}(g_{11}|\psi_1|^2 + g_{12}|\psi_2|^2, g_{12}|\psi_1|^2 + g_{22}|\psi_2|^2)$, where $g_{ij} = 4\pi a_{ij}/m$ ($i, j \in \{1, 2\}$) denotes the intra-species interaction strengths (g_{11}, g_{22}) or the inter-species interaction strength (g_{12}), with a_{ij} representing the corresponding s -wave scattering lengths, and m being the atomic mass. For simplicity,

we assume that the intra-species interaction strengths are equal, i.e. $g_{11} = g_{22} = g$. The inter-species interaction strength is characterized by the dimensionless interaction parameter $G = g_{12}/g$. Furthermore, H_0 is the single-particle SOC Hamiltonian,

$$H_0 = \frac{1}{2m}(\hat{\mathbf{p}} - k_0\sigma_z\hat{\mathbf{e}}_x)^2 + V_{\text{trap}} - \frac{\Omega}{2}\sigma_x - \eta k_0 y\sigma_z, \quad (2)$$

where k_0 is the momentum transferred during the two-photon Raman process, $\sigma_{x,y,z}$ are the usual 2×2 Pauli matrices, $V_{\text{trap}} = \frac{m}{2}(\omega_x^2 x^2 + \omega_y^2 y^2 + \omega_z^2 z^2)$ is the 3D harmonic potential with trapping frequencies of $\omega_{x,y,z}$, and Ω represents the Raman coupling strength. Additionally, η represents the gradient of the position-dependent detuning, given by $\delta(y) = -\eta k_0 y$. In general, when a position-dependent detuning $\delta(\mathbf{r})$ is present, the lower band of the SOC BEC Hamiltonian can be approximated as:

$$H \simeq \frac{(\mathbf{p} - A_x^*(\mathbf{r})\hat{\mathbf{e}}_x)^2}{2m}, \quad (3)$$

where $A_x^*(\mathbf{r}) = k_{\text{min}}(\delta(\mathbf{r}))$ acts as a synthetic vector potential. The synthetic magnetic field, defined as the curl of the synthetic vector potential, is expressed as:

$$\mathbf{B}_{\text{syn}} = \partial_z A_x^* \hat{\mathbf{e}}_y - \partial_y A_x^* \hat{\mathbf{e}}_z. \quad (4)$$

When the detuning depends only on y , as discussed in Sec. III and Sec. IV, the resulting synthetic magnetic field \mathbf{B}_{syn} points in the z -direction. This field generates a rotational velocity field in the x - y plane, imparting nonzero angular momentum to the BEC. Conversely, when the detuning depends on both y and z , as discussed in Sec. V, the resulting synthetic field can point to any arbitrary direction in the y - z plane. When η exceeds a critical value η_c , vortices form in both spin components of the BEC. When η is sufficiently large, the two spin components of the BEC become separated [40].

The HD theory of superfluids offers a useful perspective for studying the equilibrium configurations and low-lying collective modes of BEC [21, 57]. Starting from Eq. (1), we express the order parameter as $\psi = (\sqrt{n_1}e^{i\phi_1}, \sqrt{n_2}e^{i\phi_2})^T$, where n_1, ϕ_1 and n_2, ϕ_2 represent the density and phase for the two components, respectively. The HD formalism can be developed by deriving the differential equations for these new variables and performing the linearization. Due to the presence of SOC, the superfluid velocity of the condensate is fundamentally altered to $\mathbf{v}_0 = (\nabla\phi_0 - k_0 s_z \hat{\mathbf{e}}_x / n_0) / m$, where $\phi_0 = (\phi_1 + \phi_2) / 2$ represents the common phase of the two order parameters, $s_z = n_1 - n_2$ denotes the spin density, and $n_0 = n_1 + n_2$ is the total density. To simplify our analytical results, we focus on the zero-momentum phase characterized by $\Omega > \Omega_c$ with isotropic interactions ($G = 1$). Here, $\Omega_c = 4E_r$ is the critical value of the Raman coupling that marks the transition from the zero-momentum phase to the plane-wave phase and $E_r = k_0^2 / (2m)$ denotes the recoil energy. When the detuning coefficient η is small, the Thomas-Fermi (TF)

distribution can be used to approximate the total density. Thus, at equilibrium, the total density is given by $n_0 = (\mu - V_{\text{trap}})/g$, where μ is the chemical potential. The phase ϕ_0 and spin density s_z are determined as

$$\phi_0 = \alpha xy, \quad s_z = 2\beta y n, \quad (5)$$

with α and β given by $\alpha = (2\eta k_0^2 \omega_x^2)/(\Omega \omega_{xy}^2)$ and $\beta = \eta k_0(\omega_x^2 + \omega_y^2)/(\Omega \omega_{xy}^2)$ [39]. Here, $\omega_{xy} = \sqrt{(m/m^*)\omega_x^2 + \omega_y^2}$ represents the oscillation frequency of the scissors mode xy in the absence of the synthetic magnetic field. Furthermore, the superfluid velocity field \mathbf{v}_0 exhibits a rigid-body rotation form: $\mathbf{v}_0 = (-\omega_{\text{eff}}y, \omega'_{\text{eff}}x, 0)$. Here, ω_{eff} and ω'_{eff} are effective frequencies characterizing the system's rotational behavior, with $\omega_{\text{eff}} = \eta\Omega_c/\Omega - \alpha/m^*$, $\omega'_{\text{eff}} = \alpha/m$, and $m^* = m(1 - \Omega_c/\Omega)^{-1}$ representing the effective mass in the zero-momentum phase. This rigid-like rotational velocity field induces coupling between various collective modes [39, 40], resulting in intriguing dynamical phenomena.

To study collective modes, one can introduce variations in density and phase around their equilibrium configurations, represented as $n = n_0 + \delta n$ and $\phi = \phi_0 + \delta\phi$, to derive the corresponding oscillation equations. We assume that the spatial variations in density are smooth not only at equilibrium but also in low-excited states, thereby allowing the quantum pressure term to be effectively neglected. The linearized HD equations for fluctuations in density and phase can be derived as [39, 40]:

$$\begin{aligned} & \frac{\partial \delta n}{\partial t} + \frac{1}{m^*} \nabla_x [n_0 \nabla_x (\delta\phi)] + \frac{1}{m} \nabla_y [n_0 \nabla_y (\delta\phi)] \\ & + \frac{1}{m} \nabla_z [n_0 \nabla_z (\delta\phi)] - \omega_{\text{eff}} y \nabla_x (\delta n) + \omega'_{\text{eff}} x \nabla_y (\delta n) = 0, \\ & \frac{\partial \delta\phi}{\partial t} + g \delta n - \omega_{\text{eff}} y \nabla_x \delta\phi + \omega'_{\text{eff}} x \nabla_y \delta\phi = 0. \end{aligned} \quad (6)$$

By setting various ansatz forms for fluctuations in density and phase, different mode excitations can be studied, which makes the analysis more intuitive. In the following sections, we focus on the coupling between the quadrupole modes.

III. QUADRUPOLE MODES

Oscillatory behavior related to the deformation and rotation of an atomic cloud is connected with the superfluidity of BEC. The phenomenon is effectively described by quadrupole modes, which can be categorized into two types [47–49]: the diagonal quadrupole modes, represented by the operators x^2 , y^2 and z^2 , corresponding to oscillations in the overall shape of the condensate; and the scissors modes, represented by the operators xy , xz and yz , corresponding to angular rotations of the condensate within a plane. For the SOC system, these modes have been used to detect the Hall effect of superfluid in the experimental system [50]. The introduction of the synthetic magnetic field leads to the coupling of these six modes. Previous research has primarily concentrated on a specific parameter regime where the dipole modes in the plane perpendicular to the synthetic magnetic field are degenerate [39]. This article aims to conduct a more systematic study on this phenomenon.

In the framework of HD theory, to investigate the quadrupole modes, we express the density and relative phase fluctuations as quadratic polynomials, which enables us to obtain analytical solutions to Eq. (6). The ansatz for these fluctuations can be written as:

$$\begin{aligned} \delta n = & \epsilon_1 \frac{xy}{R_x R_y} + \epsilon_2 \frac{x^2}{R_x^2} + \epsilon_3 \frac{y^2}{R_y^2} + \epsilon_4 \frac{z^2}{R_z^2} \\ & + \epsilon_5 \frac{xz}{R_x R_z} + \epsilon_6 \frac{yz}{R_y R_z}, \\ \delta\phi = & g \left(\alpha_1 \frac{xy}{R_x R_y} + \alpha_2 \frac{x^2}{R_x^2} + \alpha_3 \frac{y^2}{R_y^2} + \alpha_4 \frac{z^2}{R_z^2} \right. \\ & \left. + \alpha_5 \frac{xz}{R_x R_z} + \alpha_6 \frac{yz}{R_y R_z} \right), \end{aligned} \quad (7)$$

where $R_\nu = \sqrt{2\mu_0/m\omega_\nu^2}$ represents the TF radius along the ν -direction ($\nu = x, y, z$). ϵ_i and α_i are the coefficients of corresponding excitation modes. Substituting the perturbation ansatz Eq. (7) into Eq. (6) and collecting terms with the same polynomial degree, we require that the coefficients of all independent polynomials vanish for Eq. (6) to be satisfied. This procedure results in 12 first-order differential equations for the coefficients ϵ_i and α_i :

$$\begin{aligned}
\frac{d\epsilon_1}{dt} &= \omega_{xy}^2 \alpha_1 + 2\omega_\eta \epsilon_2 - 2\omega_\eta \epsilon_3, & \frac{d\alpha_1}{dt} &= 2\omega_\eta \alpha_2 - 2\omega_\eta \alpha_3 - \epsilon_1, \\
\frac{d\epsilon_2}{dt} &= 3\frac{m}{m^*} \omega_x^2 \alpha_2 + \omega_y^2 \alpha_3 + \omega_z^2 \alpha_4 - \omega_\eta \epsilon_1, & \frac{d\alpha_2}{dt} &= -\omega_\eta \alpha_1 - \epsilon_2, \\
\frac{d\epsilon_3}{dt} &= \frac{m}{m^*} \omega_x^2 \alpha_2 + 3\omega_y^2 \alpha_3 + \omega_z^2 \alpha_4 + \omega_\eta \epsilon_1, & \frac{d\alpha_3}{dt} &= \omega_\eta \alpha_1 - \epsilon_3, \\
\frac{d\epsilon_4}{dt} &= \frac{m}{m^*} \omega_x^2 \alpha_2 + \omega_y^2 \alpha_3 + 3\omega_z^2 \alpha_4, & \frac{d\alpha_4}{dt} &= -\epsilon_4, \\
\frac{d\epsilon_5}{dt} &= \omega_{xz}^2 \alpha_5 - \omega_\eta \epsilon_6, & \frac{d\alpha_5}{dt} &= -\omega_\eta \alpha_6 - \epsilon_5, \\
\frac{d\epsilon_6}{dt} &= \omega_{yz}^2 \alpha_6 + \omega_\eta \epsilon_5, & \frac{d\alpha_6}{dt} &= \omega_\eta \alpha_5 - \epsilon_6,
\end{aligned} \tag{8}$$

where we defined a new frequency $\omega_\eta \equiv \omega_{eff} \omega_x / \omega_y = \omega'_{eff} \omega_y / \omega_x$, which characterises the coupling strength between these modes.

In the absence of a synthetic magnetic field ($\eta = 0$), the three scissors modes in Eq. (8) are completely decoupled and the BEC exhibits independent harmonic motion in space, with the frequencies given by $\omega_{xy} = \sqrt{(m/m^*)\omega_x^2 + \omega_y^2}$, $\omega_{xz} = \sqrt{(m/m^*)\omega_x^2 + \omega_z^2}$, and $\omega_{yz} = \sqrt{\omega_y^2 + \omega_z^2}$. However, the diagonal quadrupole modes are still coupled together but no longer couple with the scissors mode. The coupling between quadrupole modes is described by the following set of equations:

$$\begin{aligned}
\frac{\partial^2 \epsilon_2}{\partial t^2} + 3\frac{m}{m^*} \omega_x^2 \epsilon_2 + \omega_y^2 \epsilon_3 + \omega_z^2 \epsilon_4 &= 0, \\
\frac{\partial^2 \epsilon_3}{\partial t^2} + \frac{m}{m^*} \omega_x^2 \epsilon_2 + 3\omega_y^2 \epsilon_3 + \omega_z^2 \epsilon_4 &= 0, \\
\frac{\partial^2 \epsilon_4}{\partial t^2} + \frac{m}{m^*} \omega_x^2 \epsilon_2 + \omega_y^2 \epsilon_3 + 3\omega_z^2 \epsilon_4 &= 0.
\end{aligned} \tag{9}$$

Solving Eq. (9) yields the eigenfrequencies ($\omega_{1,2,3}$) of the three diagonal quadrupole modes. Figure 1 shows the dependence of these eigenfrequencies (purple curves) on Ω and x -direction trapping frequency ω_x . It is worth noting that in the presence of SOC and the synthetic magnetic field ($\eta \neq 0$), only the scissors mode in the x - y plane can couple with the diagonal quadrupole modes, while the other two scissors modes xz and yz are not involved.

The frequency ω_{xy} represented by the red curve is also shown in Figs. 1(a)-1(d). The crossing points between the curves are marked with green stars and blue circles to distinguish two sets of system parameters, for which the eigenfrequencies [Eq. (9)] of the diagonal quadrupole modes and the scissors mode frequency ω_{xy} become degenerate. For the case mentioned above, this corresponds to the following two degeneracy conditions:

$$\sqrt{\frac{m}{m^*}} \omega_x = \omega_y, \tag{10a}$$

$$\omega_z = \sqrt{\frac{2}{5} \left(\frac{m}{m^*} \omega_x^2 + \omega_y^2 \right)}. \tag{10b}$$

Under the first degeneracy condition [Eq. (10a)], the modes in the x - y plane couple together, specifically, the scissors mode xy directly interacts with the superposed mode $Q_1 = (\omega_x/\omega_y)x^2 - (\omega_y/\omega_x)y^2$. This has been studied in the previous work [39]. Yet, when the second degeneracy condition [Eq. (10b)] is satisfied, all four modes, including xy , x^2 , y^2 and z^2 , are coupled, and the specific manifestation of this coupling has not been investigated. We examine two scenarios corresponding to Raman coupling strength at $\Omega = 6E_r$ [Figs. 1(a) and 1(b)] and $\Omega = 7E_r$ [Figs. 1(c) and 1(d)], respectively. These values are far from the phase transition point Ω_c from the single-minimum phase to the plane-wave phase, also making them convenient for GPE simulation. Under these conditions, we observe that there is only one crossing point in Fig. 1(a), indicating that only the second degeneracy can occur. In Figs. 1(a)-1(d), crossing points correspond to the first and the second degeneracy conditions. We next analyze the second degeneracy case.

A. Coupling between xy , x^2 , y^2 and z^2

Bringing the second degeneracy condition [Eq. (10b)] into Eq. (9), one of the eigenfrequencies is equal to the scissors mode frequency ω_{xy} in magnitude (blue circles in Fig. 1). This result indicates that there is a mode referred to as Q_2 , expressed as a superposition of three coefficients $\epsilon_{1,2,3}$:

$$\langle Q_2 \rangle = -\frac{1}{5} \frac{\frac{m}{m^*} \omega_x^2 + \omega_y^2}{\frac{m}{m^*} \omega_x^2 - \omega_y^2} (\epsilon_2 - \epsilon_3) + \epsilon_4. \tag{11}$$

Using the ansatz δn from Eq. (7), solving inversely for the three coefficients $\epsilon_{2,3,4}$ yields their forms in terms of the three measurable quantities x^2 , y^2 and z^2 . The relationships between the coefficients and the measurable

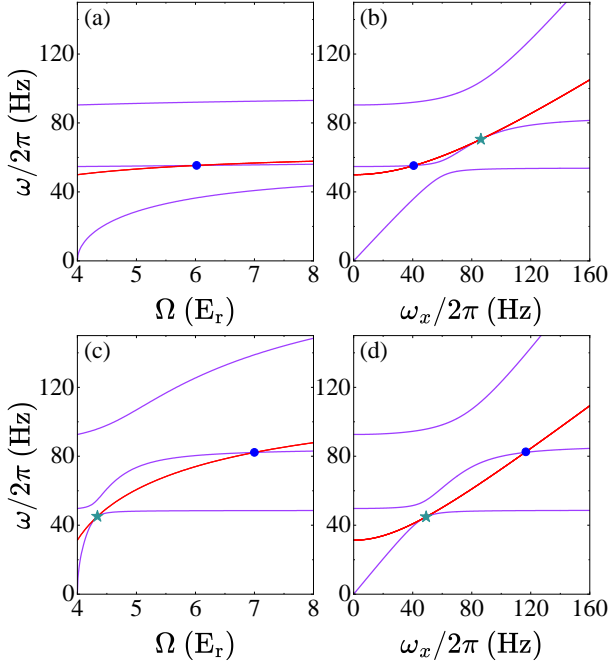


FIG. 1. The dependence of the eigenfrequencies $\omega_{1,2,3}$ (purple curves) of Eq. (9) and the frequency ω_{xy} (red curves) on Raman coupling strength Ω and x -direction trapping frequency ω_x . The red line can intersect a purple line in various ways. Panel (a) shows a single intersection where ω_{xy} meets ω_2 once. Panel (b) presents intersecting twice between ω_{xy} and ω_2 . In panels (c) and (d), ω_{xy} crosses each of ω_2 and ω_3 once, yielding two cross points per panel. Overall, there can be one intersection (a), two intersections (b), or intersections with two purple lines as in panels (c) and (d). In these four panels, green stars (★) represent points satisfying the first degeneracy condition [Eq. (10a)], while blue circles (●) represent points satisfying the second degeneracy condition [Eq. (10b)]. For panel (a) [(c)], the parameters are set to $(\omega_x, \omega_y, \omega_z) = (41.08, 50, 35) \times 2\pi$ Hz [(116.13, $14\sqrt{5}$, 52) $\times 2\pi$ Hz], while for panel (b) [(d)], they are adjusted to $(\omega_y, \omega_z) = (50, 35) \times 2\pi$ Hz [(14 $\sqrt{5}$, 52) $\times 2\pi$ Hz] with $\Omega = 6E_r$ ($7E_r$).

quantities are as follows:

$$\begin{aligned} \epsilon_2 &= \frac{2}{5} \frac{\omega_x}{\omega_y} \langle x^2 \rangle - \frac{1}{10} \frac{\omega_y}{\omega_x} \langle y^2 \rangle - \frac{1}{10} \frac{\omega_z^2}{\omega_x \omega_y} \langle y^2 \rangle, \\ \epsilon_3 &= -\frac{1}{10} \frac{\omega_x}{\omega_y} \langle x^2 \rangle + \frac{2}{5} \frac{\omega_y}{\omega_x} \langle y^2 \rangle - \frac{1}{10} \frac{\omega_z^2}{\omega_x \omega_y} \langle y^2 \rangle, \\ \epsilon_4 &= -\frac{1}{10} \frac{\omega_x}{\omega_y} \langle x^2 \rangle - \frac{1}{10} \frac{\omega_y}{\omega_x} \langle y^2 \rangle + \frac{2}{5} \frac{\omega_z^2}{\omega_x \omega_y} \langle y^2 \rangle, \end{aligned} \quad (12)$$

where $\langle \cdot \rangle$ represents an average with respect to the density fluctuations δn . Substituting Eq. (12) into Eq. (11), we can obtain the operator form corresponding to the Q_2 mode as follows:

$$Q_2 = \frac{(m\omega_x^3)/(m^*\omega_y)x^2 - (\omega_y^3/\omega_x)y^2}{5(\omega_y^2 - m\omega_x^2/m^*)} + \frac{4\omega_{xy}^2}{25\omega_x\omega_y}z^2. \quad (13)$$

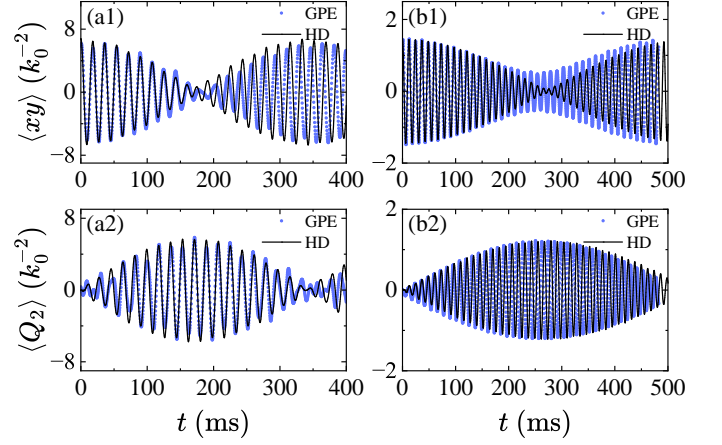


FIG. 2. Time evolution of the scissors mode $\langle xy \rangle$ and the superposed quadrupole mode $\langle Q_2 \rangle$ obtained from GPE numerical simulation (dots) and HD theory (solid lines) in the presence of a detuning gradient $\eta = 0.001E_r$. For (a1-a2) [(b1-b2)], the Raman coupling strength is $\Omega = 6E_r$ ($7E_r$), and the trapping frequency is set as $(\omega_x, \omega_y, \omega_z) = (41.08, 50, 35) \times 2\pi$ Hz [(116.13, $14\sqrt{5}$, 52) $\times 2\pi$ Hz]. The dynamics in panel (a) [panel (b)] correspond to the blue circles in Figs. 1(a) and 1(b) [Figs. 1(c) and 1(d)]. In our simulation, the parameter of the particle number $N = 2 \times 10^4$ was used, and this parameter remained unchanged in the subsequent simulations. The system's dynamics are initiated by an abrupt rotation on the harmonic trap with a slight angle $\varphi_0 = 3^\circ$ in the x - y plane.

Following the same procedure, the average of the scissors mode xy is expressed as

$$\langle xy \rangle = \frac{4}{105} \pi R_x^2 R_y^2 R_z \epsilon_1. \quad (14)$$

Introducing a weak synthetic magnetic field ($\eta = 0.001E_r$) couples two independent modes, Q_2 and xy , breaking the second degeneracy condition. By rotating the BEC by a small angle around the z -axis, the xy mode is excited. The subsequent dynamics of the two modes (xy and Q_2) exhibits a characteristic beating effect. Figure 2 shows the coupling between the scissors mode xy and the superposed mode Q_2 . The black lines and blue dots, which are the results of HD theory and GPE simulation respectively, are in good agreement. The black lines and blue dots, which are the results of HD theory and GPE simulation respectively, are in good agreement. The discrepancy observed in Fig. 2(b1) near the beat node arises from the finite particle number. We have verified that as the particle number N increases, the system approaches the TF approximation more closely, and these mismatches are significantly reduced. Comparing Figs. 2(a) and 2(b), the beat frequency when $\Omega = 6E_r$ is larger than that when $\Omega = 7E_r$, indicating stronger mode coupling in the former case. This is because increasing the Raman coupling strength Ω weakens the effective synthetic magnetic field.

B. Coupling between scissors modes xz and yz

In the previous subsection, we explored the coupling among four quadrupole modes. Now, we turn our attention to the remaining two scissors modes, xz and yz , which also couple under the second degeneracy condition. In the absence of a synthetic magnetic field ($\eta = 0$), the first degeneracy condition [Eq. (10a)] implies $\omega_{xz} = \omega_{yz}$. However, under the second degeneracy condition [Eq. (10b)], $\omega_{xz} \neq \omega_{yz}$, no degeneracy occurs between these two modes. Introducing a weak synthetic magnetic field ($\eta = 0.001E_r$) will cause these two modes coupling together regardless of whether their frequencies are equal or not. The response of the system differs depending on whether the frequencies are degenerate. In the following, we will analyze the case where $\omega_{xz} \neq \omega_{yz}$, and these two scissors modes are non-degenerate.

Rotating the BEC around the y -axis excites the xz mode, while rotating around the x -axis excites the yz mode. From Eq. (8), we derive the coupling equations for these two modes as follows:

$$\begin{aligned} \frac{d^2 \epsilon_5}{dt^2} + \omega_{xz}^2 \left(1 - \frac{\omega_\eta^2}{\omega_{yz}^2}\right) \epsilon_5 + \omega_\eta \left(1 + \frac{\omega_{xz}^2}{\omega_{yz}^2}\right) \frac{d\epsilon_6}{dt} &= 0, \\ \frac{d^2 \epsilon_6}{dt^2} + \omega_{yz}^2 \left(1 - \frac{\omega_\eta^2}{\omega_{xz}^2}\right) \epsilon_6 - \omega_\eta \left(1 + \frac{\omega_{yz}^2}{\omega_{xz}^2}\right) \frac{d\epsilon_5}{dt} &= 0, \end{aligned} \quad (15)$$

where the coefficients are determined by ω_{xz} , ω_{yz} , and ω_η . It is worth noting that if $\omega_{xz} = \omega_{yz}$, the coefficients for ϵ_5 and ϵ_6 become identical, satisfying the first degeneracy condition. In this degenerate case, the motion is linked to a BEC gyroscope as discussed in Ref. [40]. Additionally, similar coupling structures can also be observed in the dipole modes of the system, where the motion resembles a Foucault pendulum in the x - y plane, as reported in Ref. [39]. When $\omega_{xz} \neq \omega_{yz}$, the trajectories of the two modes form various Lissajous-like patterns in the $\langle xz \rangle$ - $\langle yz \rangle$ parameter space.

We adopt three excitation methods to generate these Lissajous-like patterns: (i) Rotation around the y -axis, corresponding to $\epsilon_5 = 1$, $\epsilon_6 = 0$ in the HD theory. (ii) Rotation around the x -axis, corresponding to $\epsilon_5 = 0$, $\epsilon_6 = 1$. (iii) Successive rotations around the x - and y -axes, corresponding to $\epsilon_5 = 1$ and $\epsilon_6 = 1$. Figure 3 shows the resulting Lissajous-like patterns generated by these three methods, with the HD theory and GPE simulations showing good agreement in their spatial paths.

Under the second degeneracy condition [Eq. (10b)], the two scissors modes xz and yz are generally not degenerate, except when $\sqrt{m/m^*}\omega_x = \omega_y$. As shown in Eq. (15), the detuning gradient η induces a coupling between these two modes. However, due to the significant frequency gap between them, the coupling remains weak, resulting in only small perturbations to their independent dynamics. This weak coupling leads to distinct Lissajous-like patterns, which depend sensitively on the initial conditions. The dominant mode in the

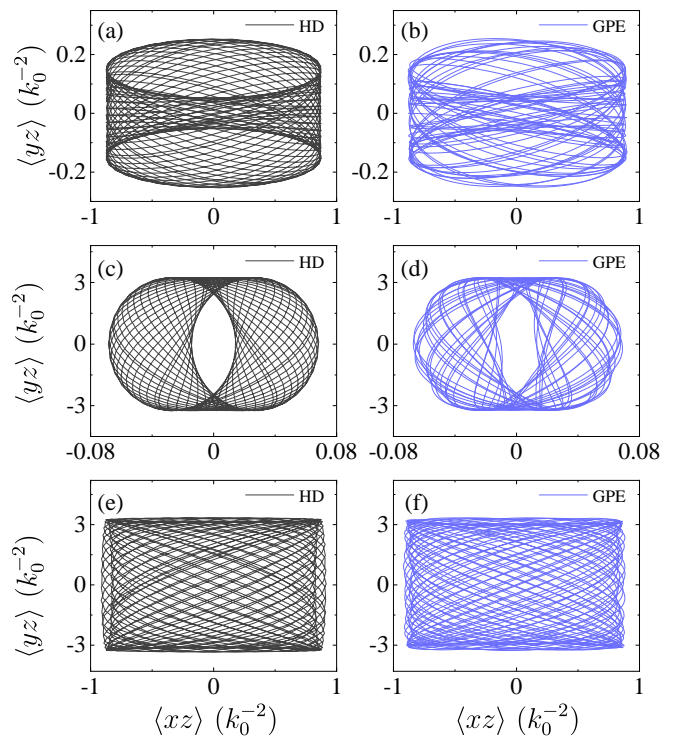


FIG. 3. Illustration of the Lissajous-like patterns obtained from HD theory (left) and GPE simulations (right). The system parameters are chosen as $(\omega_x, \omega_y, \omega_z) = (116.13, 14\sqrt{5}, 52) \times 2\pi$ Hz, and $\Omega = 7E_r$, fulfilling the condition indicated by blue circles \bullet in Figs. 1(c) and 1(d). Panels (a), (c) and (d) depict the parameters with initial set $(\epsilon_5, \epsilon_6) = (1, 0)$, $(0, 1)$ and $(1, 1)$, while panels (b), (d) and (f) show the GPE simulation. In the GPE simulation, panel (b) depicts an abrupt 3° rotation in the x - z plane, induced by rotating the harmonic trap. Panel (d) shows a similar 3° rotation in the y - z plane. Panel (f) illustrates a superposed rotation of 3° in both the x - z and y - z planes.

dynamics can be identified from both the amplitude of the time evolution and the weights of the peaks in the Fourier spectrum. For instance, when the $\langle xz \rangle$ mode is initially excited with a large amplitude, the Fourier spectrum is dominated by the frequency component ω_{xz} with a secondary, weaker peak near ω_{yz} [see Fig. 3(a)-(b)]. Conversely, when the $\langle yz \rangle$ mode is primarily excited, the Fourier spectrum exhibits a dominant frequency component at ω_{yz} , accompanied by a smaller peak appears near ω_{xz} [see Fig. 3(c)-(d)]. When both modes are equally excited, two prominent peaks with similar weights appear in the Fourier spectrum [Fig. 3(e)-(f)]. The substantial frequency difference between the two modes modifies the coefficients in the coupling equations, thereby preventing the emergence of a perfect beating effect [58]. Instead, the weak interaction between the two modes gives rise to distinct Lissajous-like patterns, highlighting the interplay between the two modes and the role of detuning-gradient-induced coupling.

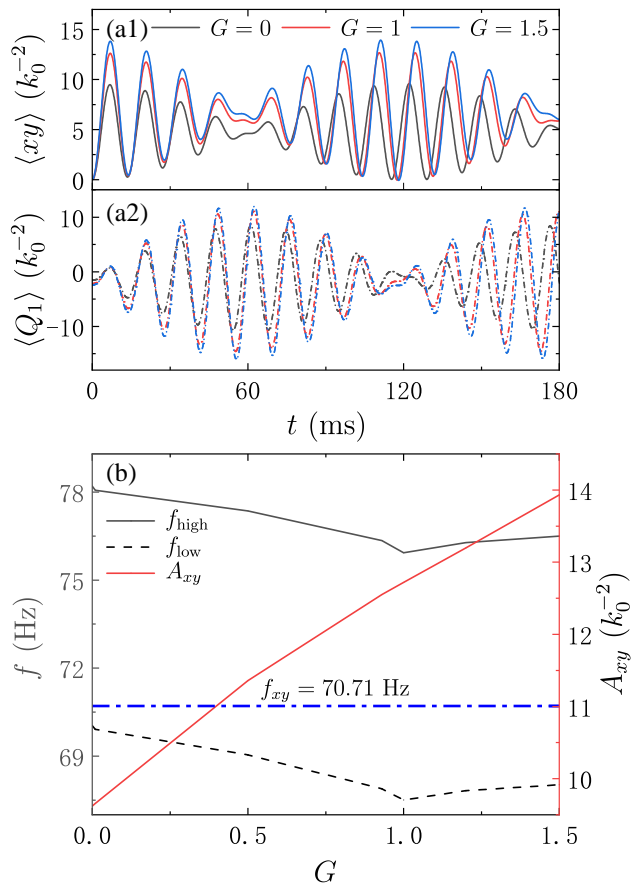


FIG. 4. Panels (a1-a2) shows three sets of beat patterns of the scissors mode xy and the superposed mode Q_1 under different interaction parameters ($G = 0, 1, 1.5$), displayed in different colors. The system parameters are chosen as $(\omega_x, \omega_y, \omega_z) = (50\sqrt{3}, 50, 35) \times 2\pi$ Hz and $\Omega = 6E_r$, ensuring the first degeneracy condition [Eq. (10a)] is met. In panel (b), the black solid line and black dashed line represent the positions of two main peaks in the Fourier spectrum of the beat pattern of the scissors mode xy as the interaction (G) varies. The blue dashed line indicates the scissors mode frequency ($f_{xy} = 70.71$ Hz) obtained using HD theory in the absence of synthetic magnetic field ($\eta = 0$) and $G = 1$. The red solid line represents the envelope function amplitude A_{xy} of the scissors mode xy as a function of G , showing a linear relationship. The dynamics are initiated by abruptly rotating the harmonic trap by a small angle $\phi_0 = 3^\circ$ in the x - y plane.

IV. EFFECT OF THE ANISOTROPIC INTERACTION

In this section, we explore how anisotropic interactions affect the coupling between quadrupole modes, specifically under the first degeneracy condition [Eq. (10a)]. The synthetic magnetic field breaks the initial degeneracy, coupling the xy and Q_1 modes, which leads to a beating effect. Changes in the inter-species interaction g_{12} directly impact the mode frequencies and amplitudes, reflecting shifts in the system's energy distribution.

For simplicity, we initially assume isotropic interac-

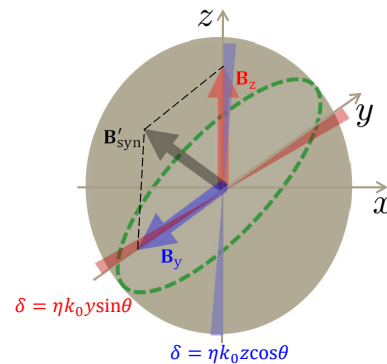


FIG. 5. Illustration of the synthetic magnetic field for a BEC with the detuning dependent on both the y and z positions. Specifically, y (z)-position dependent detuning generate a $+z$ ($-y$)-direction synthetic magnetic field \mathbf{B}_z (\mathbf{B}_y) represented by red (blue) arrow. The black arrow, \mathbf{B}'_{syn} , denotes the total synthetic magnetic field resulting from the superposition of \mathbf{B}_y and \mathbf{B}_z . The green dashed line marks the plane perpendicular to \mathbf{B}'_{syn} .

tions with $g_{ij} = g$. However, the present SOC BEC experiment allows the scattering length to be tuned by the Feshbach resonance, allowing the exploration of various interaction parameters [59, 60]. In different parameter regions, SOC BEC exhibits new properties. For example, supersolid phase will appear in antiferromagnetic configuration [35, 43]. The phase separation and miscibility induced by the interaction make the ground state be a necklace state and a continuous flow state, respectively [61]. To rigorously examine the influence of anisotropic interactions, we focus on the first degeneracy condition [Eq. (10a)] and investigate how varying interaction parameter $G = g_{12}/g$ influences quadrupole mode coupling. The system parameters are set to $(\omega_x, \omega_y, \omega_z) = (50\sqrt{3}, 50, 35) \times 2\pi$ Hz and $\Omega = 6E_r$, where the scissors mode xy couples with the diagonal quadrupole mode $Q_1 = (\omega_x/\omega_y)x^2 - (\omega_y/\omega_x)y^2$. Numerical simulations reveal the time evolution of both modes.

Figure 4(a) shows the time evolution of the xy and Q_1 modes for $G = 0, 1$, and 1.5 . These modes remain coupled, indicating that the beating effect persists even when $G \neq 1$. The variation in the inter-species interaction g_{12} alters the size of the atomic cloud, causing a linear change in the envelope function amplitude A_{xy} of the scissors mode, as shown by the red solid line in Fig. 4(b). Additionally, changes in g_{12} shift the oscillation frequencies of the quadrupole modes. To highlight these frequency shifts, we performed a Fourier transform on the time-evolution data of the xy mode. In Fig. 4(b), when $\eta \neq 0$, the degeneracy is lifted, resulting in two distinct frequencies near the scissors mode frequency $f_{xy} = 70.71$ Hz (blue dashed line). The beating effect arises from the frequency difference between these two modes. We further plot the frequencies of the two dominant peaks in the spectrum, f_{high} (black solid line) and f_{low} (black dashed line), as functions of the interaction parameter.

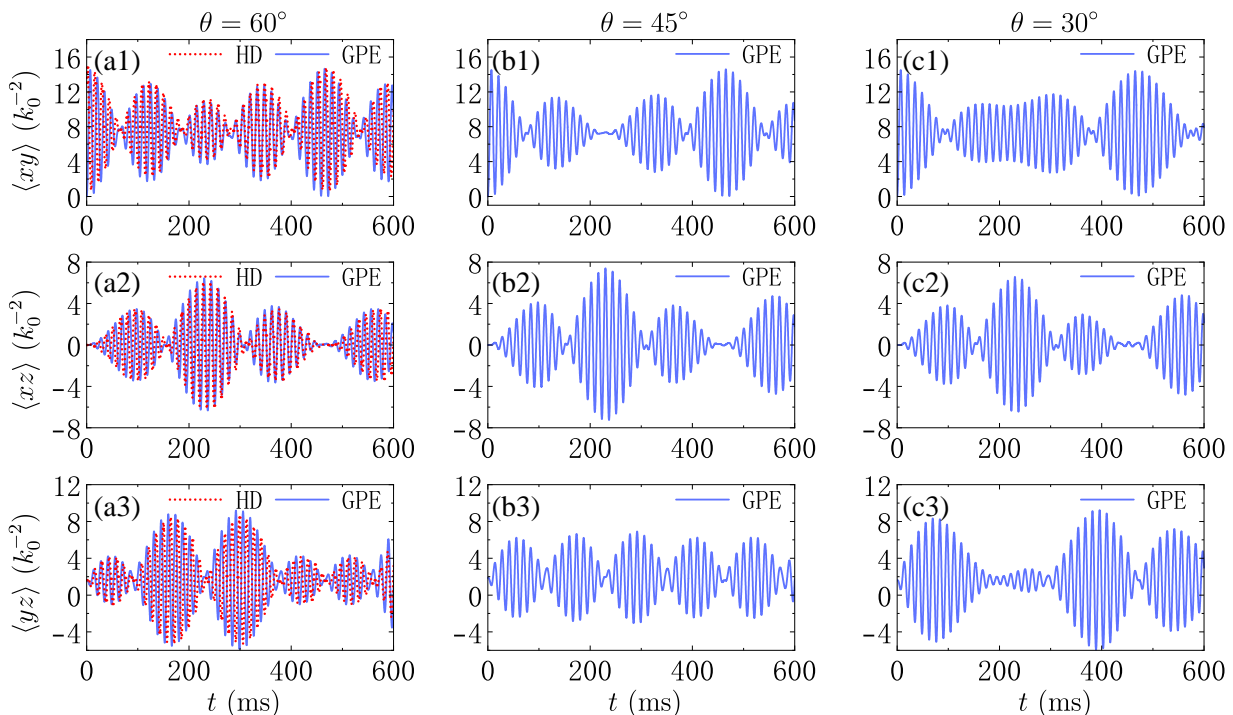


FIG. 6. Schematic representation of the scissors modes $\langle xy \rangle$, $\langle xz \rangle$, $\langle yz \rangle$ under a synthetic magnetic field applied in the y - z plane with three different gradient ratios, corresponding to $\theta = 60^\circ$ (left), $\theta = 45^\circ$ (middle) and $\theta = 30^\circ$ (right), respectively. The parameters for the GPE (blue line) and HD (red dotted line) simulations are: $(\omega_x, \omega_y, \omega_z) = (50\sqrt{3}, 50, 50) \times 2\pi$ Hz, $\Omega = 6E_r$, and $\eta = 0.001E_r$. The system's dynamics are triggered by a sudden $\varphi_0 = 3^\circ$ rotation of the harmonic trap in the x - y plane.

Both frequencies exhibit a minimum at $G = 1$.

V. EFFECT OF SYNTHETIC MAGNETIC FIELD DIRECTION

In previous sections, we examined the quadrupole mode under the influence of a synthetic magnetic field \mathbf{B}_{syn} , which originates from a detuning gradient dependent solely on the y -position. However, the detuning's position dependence can be generalized [see Eq. (4)]. In this section, we introduce a z -position-dependent term alongside the y -position-dependent term in the detuning. This generates a new synthetic magnetic field along the $-y$ direction. As illustrated in Fig. 5, the black arrows represent the total synthetic magnetic field \mathbf{B}'_{syn} induced by the modified position-dependent detuning, while the red (blue) arrows indicate the contributions from the y (z)-position-dependent terms. In this scenario, the last term in Eq. (2) is modified as follows:

$$-\eta k_0 y \sigma_z \rightarrow -\eta k_0 (y \sin \theta + z \cos \theta) \sigma_z, \quad (16)$$

where η is the coefficient of the position-dependent detuning, and θ is a dimensionless parameter that tunes the ratio between the y and z detuning components. By varying θ , we can explore how different directions of the synthetic magnetic field affect the collective mode dynamics, as shown in Eq. (A1).

When the parameter $\theta = 0^\circ$, the detuning becomes z -dependent and the synthetic magnetic field points to the y -direction. Under the first degeneracy condition [Eq. (10a)], the coupling dynamics of the three scissors modes are similar to the conclusion in Sec. III: the xz scissors mode becomes coupled to another superposed-mode $Q'_1 = (\omega_x/\omega_z)x^2 - (\omega_z/\omega_x)z^2$, and the scissors modes xy and yz are coupled together, forming a characteristic beating effect. Figure 6 illustrates the time evolution for three scissors modes under different angles θ . Specifically, for $\theta = 60^\circ$ (left), 45° (middle), and 30° (right), distinct differences in the beating patterns, both in oscillation periods and shapes, are observed. Notably, the case of $\theta = 60^\circ$ Fig. 6(a1-a3) shows excellent agreement between the generalized HD theory (see Appendix) and GPE simulations. Even minor alterations in the gradient direction lead to pronounced beating effects, underlining the high sensitivity of the system to the direction of the synthetic magnetic field. This unique property empowers the SOC BEC system not only to detect the existence of a magnetic field gradient but also to precisely ascertain its direction, thus making it a promising candidate for quantum sensing applications.

VI. CONCLUSIONS

In summary, we have conducted a systematic study of collective oscillations of SOC BEC under the position-dependent detuning. By combining HD theory with numerical simulations of the GPE, we investigated the coupling dynamics of quadrupole modes with various degeneracy conditions. We identified a superposition of diagonal quadrupole modes Q_2 coupling with the scissors mode xy , resulting in interesting beating effects. In contrast, the coupling of the scissors modes xz and yz forms trajectories reminiscent of Lissajous patterns. Additionally, we extended our studies to more general scenarios and numerically investigated the effects of anisotropic interactions and the direction of the synthetic magnetic field on the dynamics of quadrupole modes. Our results indicate that anisotropic interactions significantly affect the amplitudes and oscillation frequencies of the scissors modes. Varying the direction of the synthetic magnetic field induces a notable response from the system, with significant alterations in the beating dynamics of the scissors modes. This suggests that the system has potential as a magnetic field gradiometer for measuring the direction of magnetic field gradients. These findings not only provide new insights into the fundamental physics of SOC BEC

but also offer valuable theoretical foundations for future experimental research and application development.

ACKNOWLEDGMENTS

This work is supported by the National Natural Science Foundation of China (NSFC) under Grants No. 12374247 and No. 11974235, as well as by the Shanghai Municipal Science and Technology Major Project (Grant No. 2019SHZDZX01-ZX04). C.Q. is supported by ACC-New Jersey under Contract No. W15QKN-18-D-0040.

Appendix A: Hydrodynamic equations for synthetic magnetic field in arbitrary directions

By applying the perturbation ansatz in Eq. (7) (Sec. V), we derive 12 revised coupled equations governing the six collective modes. These equations include additional terms involving ω_{η_2} , which originate from the influence of the magnetic field pointing to an arbitrary direction in the $y-z$ plane. The complete set of equations is presented below:

$$\begin{aligned}
 \frac{d\epsilon_1}{dt} &= \omega_{xy}^2 \alpha_1 + 2\omega_{\eta_1} \epsilon_2 - 2\omega_{\eta_1} \epsilon_3 - \omega_{\eta_2} \epsilon_6, & \frac{d\alpha_1}{dt} &= 2\omega_{\eta_1} \alpha_2 - 2\omega_{\eta_1} \alpha_3 - \omega_{\eta_2} \alpha_6 - \epsilon_1, \\
 \frac{d\epsilon_2}{dt} &= 3\frac{m}{m^*} \omega_x^2 \alpha_2 + \omega_y^2 \alpha_3 + \omega_z^2 \alpha_4 - \omega_{\eta_1} \epsilon_1 - \omega_{\eta_2} \epsilon_5, & \frac{d\alpha_2}{dt} &= -\omega_{\eta_1} \alpha_1 - \omega_{\eta_2} \alpha_5 - \epsilon_2, \\
 \frac{d\epsilon_3}{dt} &= \frac{m}{m^*} \omega_x^2 \alpha_2 + 3\omega_y^2 \alpha_3 + \omega_z^2 \alpha_4 + \omega_{\eta_1} \epsilon_1, & \frac{d\alpha_3}{dt} &= \omega_{\eta_1} \alpha_1 - \epsilon_3, \\
 \frac{d\epsilon_4}{dt} &= \frac{m}{m^*} \omega_x^2 \alpha_2 + \omega_y^2 \alpha_3 + 3\omega_z^2 \alpha_4 + \omega_{\eta_2} \epsilon_5, & \frac{d\alpha_4}{dt} &= \omega_{\eta_2} \alpha_5 - \epsilon_4, \\
 \frac{d\epsilon_5}{dt} &= \omega_{xz}^2 \alpha_5 - \omega_{\eta_1} \epsilon_6 + 2\omega_{\eta_2} \epsilon_2 - 2\omega_{\eta_2} \epsilon_4, & \frac{d\alpha_5}{dt} &= -\omega_{\eta_1} \alpha_6 + \omega_{\eta_2} \alpha_2 - \omega_{\eta_2} \alpha_4 - \epsilon_5, \\
 \frac{d\epsilon_6}{dt} &= \omega_{yz}^2 \alpha_6 + \omega_{\eta_1} \epsilon_5 + \omega_{\eta_2} \epsilon_1, & \frac{d\alpha_6}{dt} &= \omega_{\eta_1} \alpha_5 + \omega_{\eta_2} \alpha_1 - \epsilon_6.
 \end{aligned} \tag{A1}$$

We have also introduced new representations to express these coupling coefficients:

$$\begin{cases} \omega_{\eta_1} = \frac{\Omega_c \eta}{\hbar \Omega} \frac{\omega_x \omega_y}{\omega_{xy}^2} \sin \theta, \\ \omega_{\eta_2} = \frac{\Omega_c \eta}{\hbar \Omega} \frac{\omega_x \omega_z}{\omega_{xz}^2} \cos \theta, \end{cases} \tag{A2}$$

where ω_{η_1} and ω_{η_2} are newly defined frequencies that characterise the coupling strength between the respective modes.

[1] M. H. Anderson, J. R. Ensher, M. R. Matthews, C. E. Wieman, and E. A. Cornell, Observation of Bose-Einstein condensation in a dilute atomic vapor, *Science* **269**, 198 (1995).

[2] K. O'hara, S. Hemmer, M. Gehm, S. Granade, and J. Thomas, Observation of a strongly interacting degenerate Fermi gas of atoms, *Science* **298**, 2179 (2002).

[3] M. Lewenstein, A. Sanpera, V. Ahufinger, B. Damski, A. Sen, and U. Sen, Ultracold atomic gases in optical lat-

- tices: mimicking condensed matter physics and beyond, *Adv. Phys.* **56**, 243 (2007).
- [4] I. Bloch, J. Dalibard, and W. Zwerger, Many-body physics with ultracold gases, *Rev. Mod. Phys.* **80**, 885 (2008).
- [5] Y.-J. Lin, R. L. Compton, A. R. Perry, W. D. Phillips, J. V. Porto, and I. B. Spielman, Bose-Einstein Condensate in a Uniform Light-Induced Vector Potential, *Phys. Rev. Lett.* **102**, 130401 (2009).
- [6] Y.-J. Lin, R. L. Compton, K. Jiménez-García, J. V. Porto, and I. B. Spielman, Synthetic magnetic fields for ultracold neutral atoms, *Nature* **462**, 628 (2009).
- [7] Y.-J. Lin, R. L. Compton, K. Jimenez-Garcia, W. D. Phillips, J. V. Porto, and I. B. Spielman, A synthetic electric force acting on neutral atoms, *Nat. Phys.* **7**, 531 (2011).
- [8] Y.-J. Lin, K. Jiménez-García, and I. B. Spielman, Spin-orbit-coupled Bose-Einstein condensates, *Nature* **471**, 83 (2011).
- [9] N. Goldman, G. Juzeliūnas, P. Öhberg, and I. B. Spielman, Light-induced gauge fields for ultracold atoms, *Rep. Prog. Phys.* **77**, 126401 (2014).
- [10] L. Huang, Z. Meng, P. Wang, P. Peng, S.-L. Zhang, L. Chen, D. Li, Q. Zhou, and J. Zhang, Experimental realization of two-dimensional synthetic spin-orbit coupling in ultracold fermi gases, *Nat. Phys.* **12**, 540 (2016).
- [11] Z. Wu, L. Zhang, W. Sun, X.-T. Xu, B.-Z. Wang, S.-C. Ji, Y. Deng, S. Chen, X.-J. Liu, and J.-W. Pan, Realization of two-dimensional spin-orbit coupling for Bose-Einstein condensates, *Science* **354**, 83 (2016).
- [12] M. Z. Hasan and C. L. Kane, Colloquium: Topological insulators, *Rev. Mod. Phys.* **82**, 3045 (2010).
- [13] J. Dalibard, F. Gerbier, G. Juzeliūnas, and P. Öhberg, Colloquium: Artificial gauge potentials for neutral atoms, *Rev. Mod. Phys.* **83**, 1523 (2011).
- [14] G. Jotzu, M. Messer, R. Desbuquois, M. Lebrat, T. Uehlinger, D. Greif, and T. Esslinger, Experimental realization of the topological Haldane model with ultracold fermions, *Nature* **515**, 237 (2014).
- [15] M. Atala, M. Aidelsburger, J. T. Barreiro, D. Abanin, T. Kitagawa, E. Demler, and I. Bloch, Direct measurement of the Zak phase in topological Bloch bands, *Nat. Phys.* **9**, 795 (2013).
- [16] M. Lohse, C. Schweizer, O. Zilberberg, M. Aidelsburger, and I. Bloch, A Thouless quantum pump with ultracold bosonic atoms in an optical superlattice, *Nat. Phys.* **12**, 350 (2016).
- [17] M. Leder, C. Grossert, L. Sitta, M. Genske, A. Rosch, and M. Weitz, Real-space imaging of a topologically protected edge state with ultracold atoms in an amplitude-chirped optical lattice, *Nat. Commun.* **7**, 13112 (2016).
- [18] N. R. Cooper, J. Dalibard, and I. B. Spielman, Topological bands for ultracold atoms, *Rev. Mod. Phys.* **91**, 015005 (2019).
- [19] X.-J. Liu, K. T. Law, and T. K. Ng, Realization of 2D Spin-Orbit Interaction and Exotic Topological Orders in Cold Atoms, *Phys. Rev. Lett.* **112**, 086401 (2014).
- [20] Q. Zhu, C. Zhang, and B. Wu, Exotic superfluidity in spin-orbit coupled Bose-Einstein condensates, *Europhys. Lett.* **100**, 50003 (2012).
- [21] G. I. Martone, Y. Li, L. P. Pitaevskii, and S. Stringari, Anisotropic dynamics of a spin-orbit-coupled Bose-Einstein condensate, *Phys. Rev. A* **86**, 063621 (2012).
- [22] W. Zheng and Z. Li, Collective modes of a spin-orbit-coupled Bose-Einstein condensate: A hydrodynamic approach, *Phys. Rev. A* **85**, 053607 (2012).
- [23] Z. Chen and H. Zhai, Collective-mode dynamics in a spin-orbit-coupled Bose-Einstein condensate, *Phys. Rev. A* **86**, 041604 (2012).
- [24] J.-Y. Zhang, S.-C. Ji, Z. Chen, L. Zhang, Z.-D. Du, B. Yan, G.-S. Pan, B. Zhao, Y.-J. Deng, H. Zhai, S. Chen, and J.-W. Pan, Collective Dipole Oscillations of a Spin-Orbit Coupled Bose-Einstein Condensate, *Phys. Rev. Lett.* **109**, 115301 (2012).
- [25] T. Ozawa, L. P. Pitaevskii, and S. Stringari, Supercurrent and dynamical instability of spin-orbit-coupled ultracold Bose gases, *Phys. Rev. A* **87**, 063610 (2013).
- [26] C. Qu, L. P. Pitaevskii, and S. Stringari, Spin-orbit-coupling induced localization in the expansion of an interacting Bose-Einstein condensate, *New J. Phys.* **19**, 085006 (2017).
- [27] J. Radić, T. A. Sedrakyan, I. B. Spielman, and V. Galitski, Vortices in spin-orbit-coupled Bose-Einstein condensates, *Phys. Rev. A* **84**, 063604 (2011).
- [28] A. L. Fetter, Vortex dynamics in spin-orbit-coupled Bose-Einstein condensates, *Phys. Rev. A* **89**, 023629 (2014).
- [29] M. Kato, X.-F. Zhang, and H. Saito, Vortex pairs in a spin-orbit-coupled Bose-Einstein condensate, *Phys. Rev. A* **95**, 043605 (2017).
- [30] X.-F. Zhou, J. Zhou, and C. Wu, Vortex structures of rotating spin-orbit-coupled Bose-Einstein condensates, *Phys. Rev. A* **84**, 063624 (2011).
- [31] H.-Y. Hui, Y. Zhang, C. Zhang, and V. W. Scarola, Superfluidity in the absence of kinetics in spin-orbit-coupled optical lattices, *Phys. Rev. A* **95**, 033603 (2017).
- [32] D. Toniolo and J. Linder, Superfluidity breakdown and multiple roton gaps in spin-orbit-coupled Bose-Einstein condensates in an optical lattice, *Phys. Rev. A* **89**, 061605 (2014).
- [33] C. Wang, C. Gao, C.-M. Jian, and H. Zhai, Spin-Orbit Coupled Spinor Bose-Einstein Condensates, *Phys. Rev. Lett.* **105**, 160403 (2010).
- [34] T.-L. Ho and S. Zhang, Bose-Einstein Condensates with Spin-Orbit Interaction, *Phys. Rev. Lett.* **107**, 150403 (2011).
- [35] Y. Li, L. P. Pitaevskii, and S. Stringari, Quantum Tricriticality and Phase Transitions in Spin-Orbit Coupled Bose-Einstein Condensates, *Phys. Rev. Lett.* **108**, 225301 (2012).
- [36] H. Hu, B. Ramachandhran, H. Pu, and X.-J. Liu, Spin-Orbit Coupled Weakly Interacting Bose-Einstein Condensates in Harmonic Traps, *Phys. Rev. Lett.* **108**, 010402 (2012).
- [37] Y.-C. Zhang, Z.-Q. Yu, T. K. Ng, S. Zhang, L. Pitaevskii, and S. Stringari, Superfluid density of a spin-orbit-coupled Bose gas, *Phys. Rev. A* **94**, 033635 (2016).
- [38] S. Stringari, Diffused Vorticity and Moment of Inertia of a Spin-Orbit Coupled Bose-Einstein Condensate, *Phys. Rev. Lett.* **118**, 145302 (2017).
- [39] C. Qu and S. Stringari, Angular Momentum of a Bose-Einstein Condensate in a Synthetic Rotational Field, *Phys. Rev. Lett.* **120**, 183202 (2018).
- [40] C. Qu, C.-H. Li, Y. P. Chen, and S. Stringari, Scissors modes of a Bose-Einstein condensate in a synthetic magnetic field, *Phys. Rev. A* **108**, 053316 (2023).
- [41] W. Zheng, Z.-Q. Yu, X. Cui, and H. Zhai, Properties of Bose gases with the Raman-induced spin-orbit coupling,

- J. Phys. B: At., Mol. Opt. Phys **46**, 134007 (2013).
- [42] C. Hamner, Y. Zhang, M. A. Khamsehchi, M. J. Davis, and P. Engels, Spin-Orbit-Coupled Bose-Einstein Condensates in a One-Dimensional Optical Lattice, *Phys. Rev. Lett.* **114**, 070401 (2015).
- [43] J.-R. Li, J. Lee, W. Huang, S. Burchesky, B. Shteynas, F. Ç. Top, A. O. Jamison, and W. Ketterle, A stripe phase with supersolid properties in spin-orbit-coupled Bose-Einstein condensates, *Nature* **543**, 91 (2017).
- [44] I. B. Spielman, Raman processes and effective gauge potentials, *Phys. Rev. A* **79**, 063613 (2009).
- [45] S. Stringari, Collective Excitations of a Trapped Bose-Condensed Gas, *Phys. Rev. Lett.* **77**, 2360 (1996).
- [46] F. Dalfovo, S. Giorgini, L. P. Pitaevskii, and S. Stringari, Theory of Bose-Einstein condensation in trapped gases, *Rev. Mod. Phys.* **71**, 463 (1999).
- [47] D. Guéry-Odelin and S. Stringari, Scissors Mode and Superfluidity of a Trapped Bose-Einstein Condensed Gas, *Phys. Rev. Lett.* **83**, 4452 (1999).
- [48] O. M. Maragò, S. A. Hopkins, J. Arlt, E. Hodby, G. Hechenblaikner, and C. J. Foot, Observation of the Scissors Mode and Evidence for Superfluidity of a Trapped Bose-Einstein Condensed Gas, *Phys. Rev. Lett.* **84**, 2056 (2000).
- [49] K. Kasamatsu, M. Tsubota, and M. Ueda, Quadrupole and scissors modes and nonlinear mode coupling in trapped two-component Bose-Einstein condensates, *Phys. Rev. A* **69**, 043621 (2004).
- [50] L. J. LeBlanc, K. Jiménez-García, R. A. Williams, M. C. Beeler, A. R. Perry, W. D. Phillips, and I. B. Spielman, Observation of a superfluid Hall effect, *Proc. Natl. Acad. Sci. USA* **109**, 10811 (2012).
- [51] J. Wang, H. Liang, Y. Li, C.-H. Li, and C. Qu, Expansion dynamics of bose-einstein condensates in a synthetic magnetic field, *Phys. Rev. A* **110**, 043307 (2024).
- [52] O. L. Berman, R. Y. Kezerashvili, G. V. Kolmakov, and L. M. Pomirchi, Spontaneous formation and nonequilibrium dynamics of a soliton-shaped bose-einstein condensate in a trap, *Phys. Rev. E* **91**, 062901 (2015).
- [53] J. Keski-Rahkonen, A. Ruhanen, E. J. Heller, and E. Räsänen, Quantum lissajous scars, *Phys. Rev. Lett.* **123**, 214101 (2019).
- [54] Y. Zhang, L. Mao, and C. Zhang, Mean-Field Dynamics of Spin-Orbit Coupled Bose-Einstein Condensates, *Phys. Rev. Lett.* **108**, 035302 (2012).
- [55] H. Zhai, Degenerate quantum gases with spin-orbit coupling: a review, *Rep. Prog. Phys.* **78**, 026001 (2015).
- [56] Y. Zhang, M. E. Mossman, T. Busch, P. Engels, and C. Zhang, Properties of spin-orbit-coupled Bose-Einstein condensates, *Front. Phys.* **11**, 1 (2016).
- [57] L. Pitaevskii and S. Stringari, Bose-Einstein Condensation and superfluidity (2016).
- [58] M. F. Bocko and R. Onofrio, On the measurement of a weak classical force coupled to a harmonic oscillator: experimental progress, *Rev. Mod. Phys.* **68**, 755 (1996).
- [59] S. L. Cornish, N. R. Claussen, J. L. Roberts, E. A. Cornell, and C. E. Wieman, Stable ^{85}Rb Bose-Einstein Condensates with Widely Tunable Interactions, *Phys. Rev. Lett.* **85**, 1795 (2000).
- [60] S. Blatt, T. L. Nicholson, B. J. Bloom, J. R. Williams, J. W. Thomsen, P. S. Julienne, and J. Ye, Measurement of Optical Feshbach Resonances in an Ideal Gas, *Phys. Rev. Lett.* **107**, 073202 (2011).
- [61] A. C. White, Y. Zhang, and T. Busch, Odd-petal-number states and persistent flows in spin-orbit-coupled Bose-Einstein condensates, *Phys. Rev. A* **95**, 041604 (2017).